ORIGINAL PAPER

Thermal boundary conditions for heat transfer analysis of bridges considering non-uniform distribution of internal air temperature by computational fluid dynamics

Lu Zhang[1,2] · Yushi Shan[1,2] · Lingfang Li[1,2] · Fei Wang[1,2] · Yong Xia[1,2]

Abstract

Heat transfer analysis has been used to calculate the temperature distribution in bridges. Thermal boundary conditions play a critical role in this analysis. However, existing studies on thermal boundary conditions simplify the air temperature inside the bridge deck as uniform, which is not realistic and thus causes inaccurate simulation results. This study proposes a new approach to thermal boundary conditions in the heat transfer analysis of bridges. For the first time, computational fluid dynamics is used to calculate non-uniform air temperatures inside the bridge deck. In addition, non-approximate heat exchange equations for long-wave radiation are also incorporated into the approach. The techniques are applied to the 1377-m main span Tsing Ma Suspension Bridge to calculate the internal air temperatures of a deck segment. Transient heat transfer analysis is then conducted to calculate the time-dependent temperature distribution of the segment. As compared with the field monitoring results, the proposed approach can simulate the temperature distribution of the bridge with an average discrepancy of 0.88 °C and is more accurately than other existing approaches.

Keywords Temperature distribution · Heat transfer analysis · Long-span suspension bridge · Thermal boundary condition · Field monitoring · Computational fluid dynamics

1 Introduction

Bridges are exposed to daily and seasonal fluctuations in ambient temperature and solar radiation [6, 25, 41]. The heat exchange between a bridge and its surrounding environment

Lu Zhang and Yushi Shan are co-first authors.

✉ Yong Xia
ceyxia@polyu.edu.hk

Lu Zhang
lu1zhang@polyu.edu.hk

Yushi Shan
yushi.shan@connect.polyu.hk

Lingfang Li
lingfang.li@connect.polyu.hk

Fei Wang
felixwf.wang@polyu.edu.hk

1 Department of Civil and Environmental Engineering, The Hong Kong Polytechnic University, Hong Kong, China

2 Joint Research Centre for Marine Infrastructure, The Hong Kong Polytechnic University, Hong Kong, China

may result in changes in the distribution of structural temperature across the bridge [29]. The non-uniform temperature distribution in the bridge will consequently generate thermal displacements and stresses and alter dynamic characteristics [1, 16, 19, 20, 24, 27]. Temperature effects on bridges have been attracting wide attention since the 1960s [5, 13, 31, 44]. Some on-site tests have shown that the effects of temperature variations on bridge responses could be more significant than operational loads [15, 34, 39, 40, 43]. Therefore, exploring the effect of temperature on bridges' behaviors is necessary [4].

Zuk [44] studied the influences of the environment on the bridge temperature distribution, which is regarded as the first study on bridge thermal behavior. Moreover, many researchers have studied the temperature effects on bridge responses [26, 34]. For example, Xia et al. [35] reported that the temperature-induced maximum vertical displacement at the mid-span of the Tsing Ma Bridge could reach 2313 mm in 1 year. Deng et al. [7] determined that the seasonal longitudinal displacement of the Runyang Bridge was about 500 mm. Li et al. [17] reviewed the thermal behaviors of beam, arch, cable-stayed, and cable-suspension bridges.

Field monitoring is an effective approach to analyzing bridge temperature effects. Xu et al. [36] established the relationship among ambient air temperature, bridge effective temperature, and bridge responses based on the field monitoring data on the Tsing Ma Suspension Bridge in Hong Kong. Gu et al. [11] analyzed the temperature change law of a long-span concrete box girder bridge section from the measurements. Hu et al. [12] analyzed the field monitoring data of the Aizhai Bridge and reported that the fluctuation of the longitudinal displacement of the bridge expansion joint was affected mainly by the temperature, and that the movement of the expansion joint showed a periodic trend.

Most field monitoring studies establish a linear regression model between bridge temperatures and responses [38]. However, because of the limited number of sensors, the bridge temperatures are available at several sensor points only but the bridge responses are related to the temperature distribution of the entire structure. Obtaining accurate temperature-induced responses requires detailed temperature distribution of the bridge, which is impractical in field monitoring exercises.

The heat transfer analysis method is an efficient numerical approach to obtain the temperature distribution of the entire bridge. The finite element (FE)-based heat transfer analysis method was developed in the 1970s. The temperature distribution of the bridge was initially assumed to be one-dimensional distribution [9] and later developed into a two-dimensional model [8]. With the rapid development of computer technologies, accurate calculations of the temperature distribution of bridges are now possible [28, 30]. Xia et al. [35] established three-dimensional FE models of the deck plate, frame, and tower of the Tsing Ma Suspension Bridge and investigated their temperature distributions and structural responses. Zhu et al. [42] proposed an accurate calculation method for the temperature distribution of cable-stayed bridges by considering the influence of wind speed, atmospheric environment, and ground thermal characteristics. Shan et al. [23] conducted an integrated heat transfer and structural analysis of the Qingzhou Bridge. The FE-based heat transfer analysis method has been proven to be effective in calculating temperature distribution of bridges.

Quantifying the thermal boundary conditions, or the heat exchange between bridge surfaces and the environment, is essential for conducting the FE-based heat transfer analysis. Several approaches have been adopted to determine the thermal boundary conditions. The most common approach is to simplify heat radiation as heat convection and adopt an equivalent air temperature and overall heat convection coefficient [3, 8, 33, 35]. However, simply equating heat radiation to heat convection introduces significant deviations, especially when the structure temperature differs obviously from the air temperature. In addition, the air flow inside the bridge girder can lead to non-uniform air temperatures in the vertical and transverse directions. For example, the air temperature close to the top deck plate is generally higher than that adjacent to the bottom in the daytime. However, almost all existing studies have treated the interior bridge temperatures as uniform and ignored the non-uniformity. Shan et al. [23] considered the non-uniform air temperatures inside the box girder of the Qingzhou Bridge, while they adopted an iterative trial-and-error approach, which was time-consuming and might be inaccurate.

To obtain accurate bridge thermal boundary conditions and temperature distributions, this study adopts computational fluid dynamics to calculate the internal airflow and non-uniform air temperature distribution inside the bridge girder. Besides, non-approximate radiation heat exchange equations are applied to calculate the heat exchange between the bridge and its surroundings. The Tsing Ma Suspension Bridge is used as the testbed. The calculated temperature distribution is compared with field measurements and three other existing approaches. The results show that the present approach is most accurate with an average difference less than 1 ℃ from the measurement.

2 Thermal analysis of bridge structures

2.1 Heat transfer theory

For a point in a bridge structure, heat flow at time t can be expressed as the following differential equation [32]:

$$\rho c \frac{\partial T}{\partial t} = k \left(\frac{\partial^2 T}{\partial x^2} + \frac{\partial^2 T}{\partial y^2} + \frac{\partial^2 T}{\partial z^2} \right), \qquad (1)$$

where ρ is the density, c is the specific heat capacity, and T is the temperature of the point. x, y, and z are the Cartesian coordinates of the point and k is the thermal conductivity. The equation can be simplified for one- or two-dimensional analysis by neglecting the insignificant temperature variation in one or two directions.

2.2 Thermal boundary conditions

There are three types of boundary conditions for the thermal analysis [18]. The first type thermal boundary condition is that the temperature on the structural boundary is known. In the second type, the heat flux is determined, while in the third type, the heat flux is proportional to the difference between ambient and structural-surface temperatures.

For a bridge exposed to the outer environment, the insignificant temperature variation along the longitudinal direction can be neglected, and the hybrid boundary condition associated with Eq. (1) can be expressed as [8]

$$k\left(\frac{\partial T}{\partial x}n_x + \frac{\partial T}{\partial y}n_y\right) + q = 0, \tag{2}$$

where n_x and n_y are the directional cosines of the outer surface of the boundary; q is heat flow per unit area, which is composed of heat convection, heat irradiation, and solar radiation, as illustrated in Fig. 1. The heat convection between the air and the bridge happens when fluid is in motion. Heat irradiation is a bidirectional process that the bridge absorbs thermal radiation from the environment, namely long-wave radiation, and also emits long-wave radiation to the environment. The solar radiation is the major heat exchange source that consists of direct, diffused, and reflected solar radiation.

2.2.1 Heat convection

Heat flow q_c induced by heat convection with air can be calculated as [8].

$$q_c = h_c(T_a - T_s), \tag{3}$$

where T_a is the air temperature adjacent to bridge surface, T_s is the structural temperature, and h_c is the heat convection coefficient of bridge surfaces with air. h_c is related to the wind condition, and different structural surfaces with diverse geometric locations are subject to different wind conditions.

The wind speed near the structural surface is generally lower than the measurement. Zhou et al. [40] adopted the reduced wind speed to calculate the heat convection coefficient according to the angle of wind incidence, as demonstrated in Eqs. (4) and (5) and Fig. 2 [10]:

$$h_c = \begin{cases} 4 \times \overline{w} + 5.6 & (\overline{w} < 5\,\mathrm{m/s}) \\ 7.15 \times \overline{w}^{0.78} & (\overline{w} \geq 5\,\mathrm{m/s}) \end{cases} \tag{4}$$

$$\overline{w} = \begin{cases} 0.8w & (\theta_w \leq 45°, \ \text{Windward side}) \\ 0.7w & (45° < \theta_w \leq 90°, \ \text{Crosswind side}), \\ 0.6w & (\theta_w > 90°, \ \text{Leeward side}) \end{cases} \tag{5}$$

where θ_w is the wind incidence angle, $\overline{w}$ and w are the wind speed before and after reduction, respectively.

2.2.2 Solar radiation

The heat flow of the exterior surface induced by solar radiation can be expressed as

$$q_s = \alpha I_s, \tag{6}$$

where α is the absorption coefficient of the surface, I_s represents the absorbed solar radiation of the bridge exterior

Fig. 1 Heat exchange of a bridge exposed to the environment
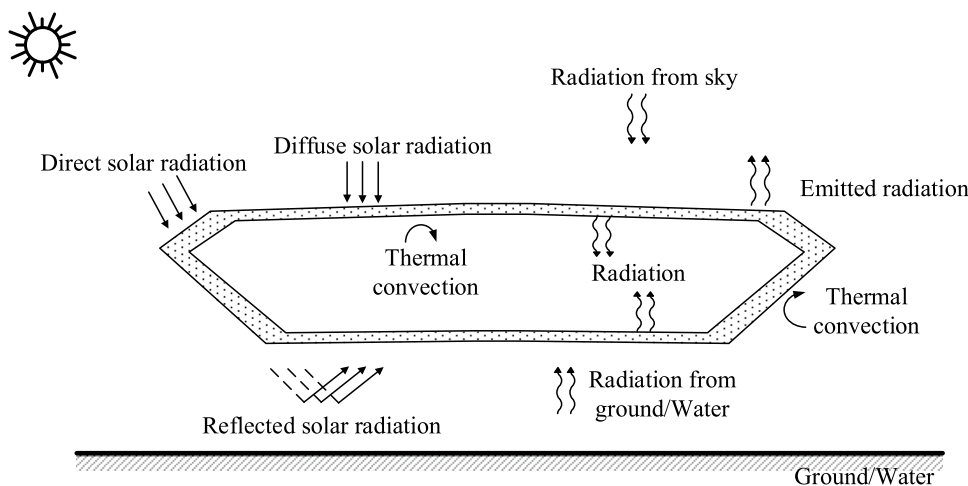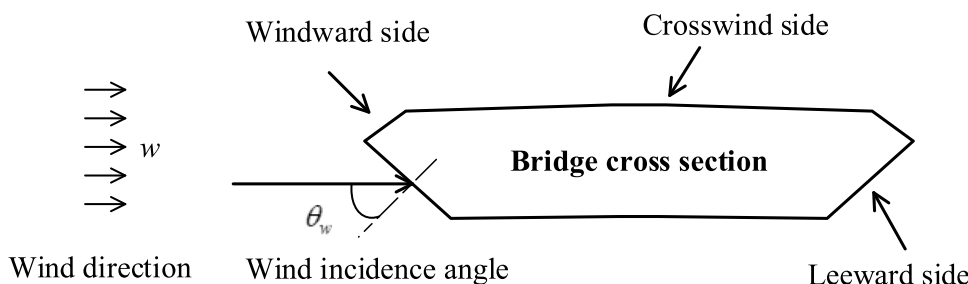

Fig. 2 Wind condition of bridge cross-section [40]

surface and consists of direct solar radiation I_{ds}, diffused solar radiation I_{ss}, and reflected solar radiation I_{rs}:

$$I_s = I_{ds} + I_{ss} + I_{rs}. \tag{7}$$

2.2.3 Long-wave radiation

Long-wave radiation exists between any objects with temperatures higher than absolute zero degree. Thus, the bridge exterior surface not only absorbs long-wave radiation from atmosphere and ground, but also emits long-wave radiation at the same time. The long-wave radiation can be calculated following Stefan–Boltzmann law:

$$G_a = \alpha \sigma T_{sky}^4 (1 + \cos \theta_i)/2, \tag{8}$$

$$G_g = \alpha \sigma \varepsilon_g T_g^4 (1 - \cos \theta_i)/2, \tag{9}$$

$$G_s = \varepsilon \sigma T_s^4, \tag{10}$$

where G_a and G_g are the radiation from the atmosphere and ground, respectively, and G_s is the emitted long-wave radiation. ε is the emissivity of bridge exterior surface, $\sigma = 5.67 \times 10^{-8}$ W/m²/K⁴ is the Stefan–Boltzmann constant, θ_i is the angle between the bridge exterior surface and the horizontal plane, ε_g is the emissivity of ground, and T_g is the ground temperature (K). T_{sky} is the effective sky temperature (K) that can be deduced from the following equations [21]:

$$T_{clear\_sky} = T_{air}(\varepsilon_{clear}^{0.25}), \tag{11}$$

$$\varepsilon_{clear} = 0.711 + 0.56(T_{dp}/100) + 0.73(T_{dp}/100)^2, \tag{12}$$

$$Ca = 1.00 + 0.0224 \times CC + 0.0035 \times CC^2 + 0.00028 \times CC^3, \tag{13}$$

$$T_{sky} = (Ca)^{0.25} T_{clear\_sky}, \tag{14}$$

where T_{clear_sky} is the effective sky temperature for clear sky (K), T_{air} is the observed air temperature (K), ε_{clear} is the emissivity of clear sky, T_{dp} is the dew point temperature (℃), Ca gives the effect of cloudiness, and CC is the cloudiness,

which is between 0 (for clear sky) and 1 (for a totally cloud sky).

The heat flow of bridge exterior surfaces induced by long-wave radiation should be expressed as

$$q_r = G_a + G_g - G_s. \tag{15}$$

For the heat radiation between bridge interior surfaces, for example, surface 1 with area of A_1 and temperature T_1 and surface 2 with area A_2 and temperature T_2, the heat flow from surface 1 to surface 2 is [2]

$$\tilde{q}_r^{12} = \frac{\sigma \varepsilon_1 \varepsilon_2 A_1 F_{12}(T_1^4 - T_2^4)}{(1 - \varepsilon_1)\varepsilon_2 A_2 F_{12} + \varepsilon_1 \varepsilon_2 A_2 + \varepsilon_1(1 - \varepsilon_2)A_1 F_{12}}, \tag{16}$$

where ε_1 and ε_2 are emissivity of surfaces 1 and 2, respectively, and F_{12} is the view factor from surface 1 to surface 2.

## 3 Case study: the Tsing Ma Suspension Bridge

3.1 Tsing Ma Suspension Bridge

The Tsing Ma Suspension Bridge is used as the testbed for calculating the temperature distribution via the heat transfer analysis. The 2132-m-long Tsing Ma Suspension Bridge is a dual-use suspension steel bridge for highways and railways. It has two carriageways on the upper deck, and two railways and two emergency carriageways on the lower deck. The bridge was opened in 1997. The main span across the Ma Wan Tower and Tsing Yi Tower is 1377 m, as shown in Fig. 3.

3.2 Temperature sensors arrangement

A structural health monitoring system of the Tsing Ma Suspension Bridge was installed and has been operating since 1997. The system includes 115 temperature sensors to monitor the temperature of the bridge as shown in Fig. 3. In particular, T1 and T2 measure bridge external and internal ambient temperatures, T3 to T5 measure the temperatures of the orthotropic deck plate and steel truss girder, and T6 to T8 measure the temperature of the main cable. The detailed

Fig. 3 Configuration and temperature sensor layout of the Tsing Ma Suspension Bridge
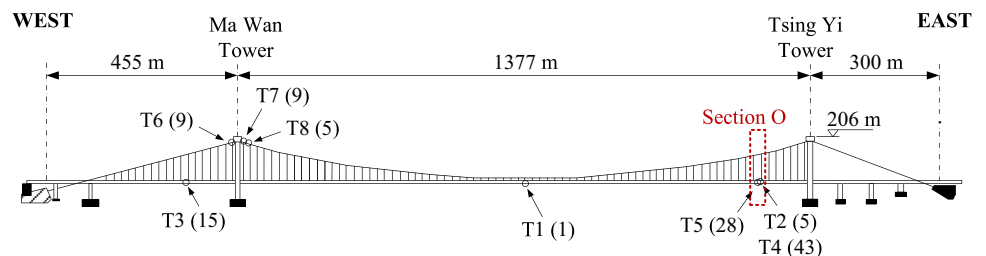
locations of all temperature sensors can be found in Xu et al. [35] and Xia et al. [36].

Figure 4 shows the detailed sensor locations in section O. Sensors D1 to D3 measure the ambient air temperature, A1 to A3 measure the temperature of the top cross frame, B1 to B3 measure the temperature of the bottom cross frame, and C1 to C4 measure the temperature of the top U trough and deck plate. The sampling frequency of temperature sensors is 0.07 Hz.

3.3 Segmental FE model for heat transfer analysis

Because the segment configuration and the thermal environment are similar along the longitudinal direction of the bridge, the longitudinal temperature variation is assumed to be negligible. A typical 18-m-long bridge segment of the bridge is chosen to perform the heat transfer analysis. The typical segment consists of a main cross frame and four intermediate cross frames with a space of 4.5 m each, connected with four longitudinal trusses, as shown in Fig. 5. Other details can be found in Xia et al. [35].

The FE model of the typical segment is established in ANSYS. It consists of 40,916 nodes and 33,295 elements. The asphalt layer, orthotropic deck, and cross frames are modeled with solid elements. The corrugated plate, cross bracing, and other components are modeled with shell elements. The material properties are listed in Table 1. The emissivity and absorptivity coefficient are related to the wavelength of radiation, with solar radiation concentrated in the short-wave band below 4 μm and thermal radiation in the long-wave band from 4 to 1000 μm. [14]. An averaged absorptivity and total emissivity coefficients from the literature [37] representing the entire wavelength range are adopted in this study as the spectral emissivity and absorptivity coefficient measurement data for the Tsing Ma Bridge are unavailable.

Two typical sunny days of July 3 and 4, 2005, with a high solar radiation intensity are selected for analysis. The measured ambient air temperature from sensors T1 and D1–D3 is shown in Figs. 6 and 7, respectively. The external ambient air temperature in Fig. 6 reached its maximum at 17:00, and the maximum solar intensity appeared around
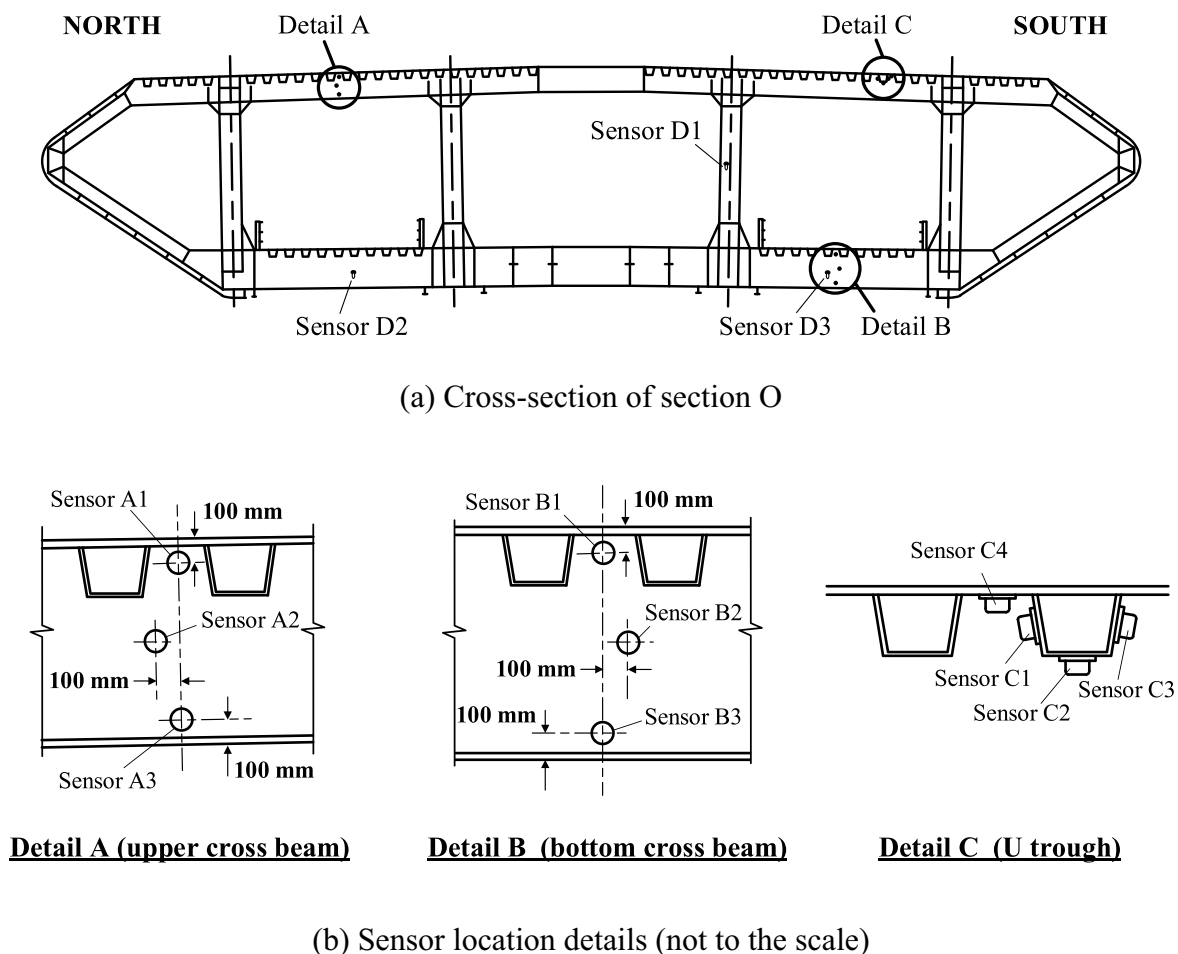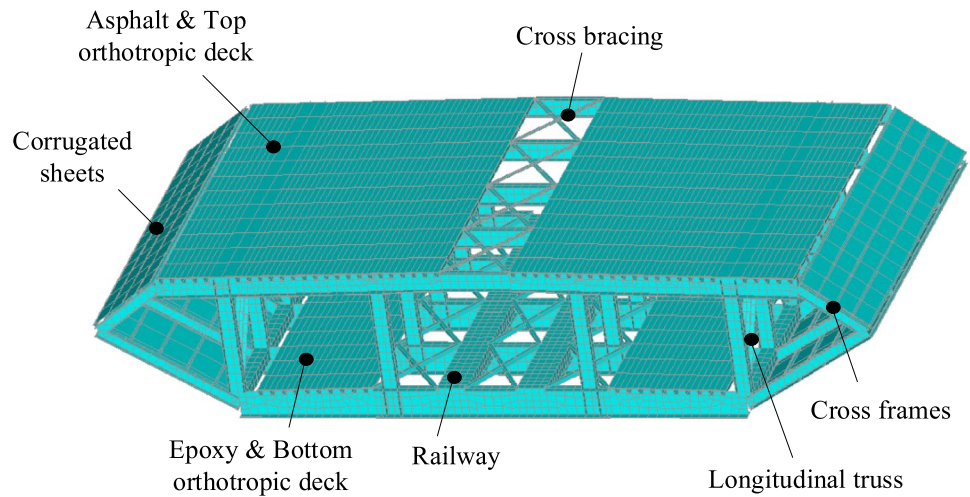

(a) Cross-section of section O

(b) Sensor location details (not to the scale)

Fig. 4 Sensor arrangement of section O. (**a**) Cross-section of section O. (**b**) Sensor location details (not to the scale)

Fig. 5 Typical segment of the Tsing Ma Bridge

Asphalt & Top orthotropic deck

Cross bracing

Corrugated sheets

Epoxy & Bottom orthotropic deck

Railway

Cross frames

Longitudinal truss

Table 1 Material properties adopted in the FE model

Parameters	Steel	Asphalt
Density ρ (kg/m³)	7850	2450
Thermal conductivity k (W/m/°C)	55	2.5
Specific heat capacity c (J/kg/°C)	460	960
Modulus of elasticity E (Pa)	2.05×10^{11}	1.3×10^9
Poisson's ratio μ	0.3	0.2
Emissivity coefficient ε	0.8	0.92
Absorptivity coefficient α	0.685	0.90

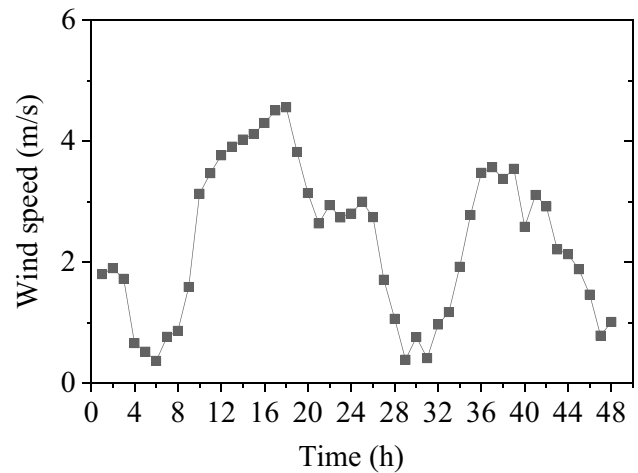**Fig. 7** Measured air temperature on July 3 and 4, 2005
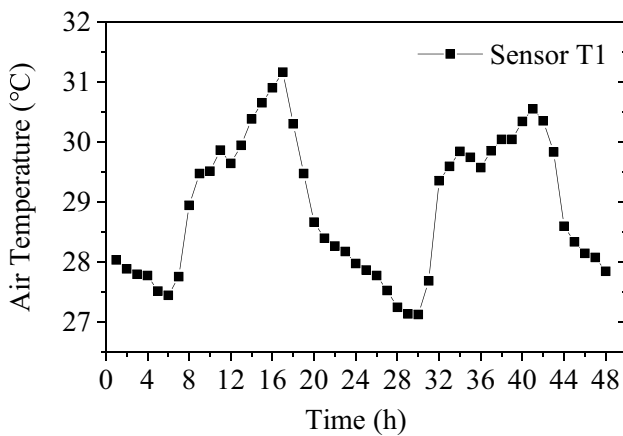
Fig. 6 Measured air temperature on July 3 and 4, 2005

13:00. Sensors D2 and D3 measure the air temperature at the bottom of the girder and reach their maximum values at 17:00, lagging from the measurement recorded by sensor D1 by approximately 2 h. The wind speed shown in Fig. 8 was measured by an ultrasonic anemometer on the bridge. Figure 9 presents the measured solar radiation intensity from the King's Park Weather Station, Hong Kong. The
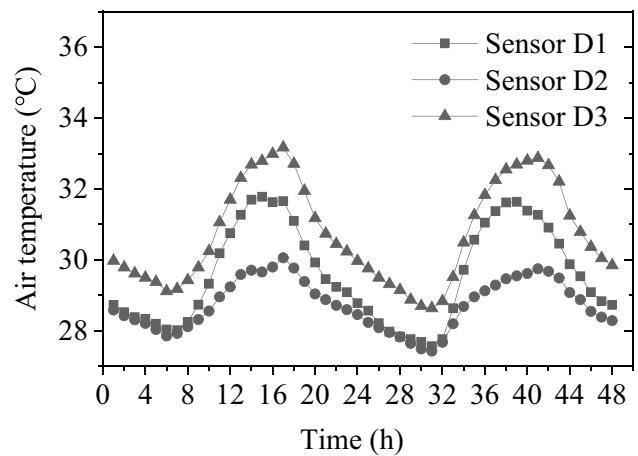
Fig. 8 Measured hourly mean wind speed on July 3 and 4, 2005
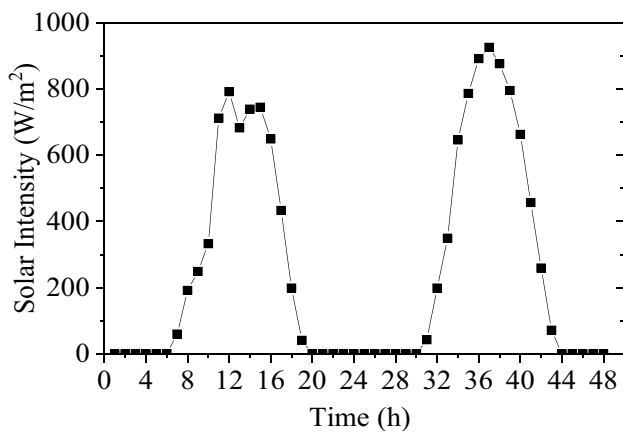
Fig. 9 Measured solar intensity on July 3 and 4, 2005

meteorological data required to calculate heat radiation from the ground and sky, such as sea surface temperature, dew point temperature, and cloud cover, are obtained from the Hong Kong Observatory (HKO). The King's Park Station and HKO are approximately 1 km apart and both are located around 12 km from the Tsing Ma Bridge.

The initial temperature condition of the bridge is assumed in line with the nighttime air temperature. Consequently, a uniform temperature field is implemented as the initial condition for the heat transfer analysis.

3.4 Two-dimensional FE model to consider air flow inside truss girder

The air temperatures along the vertical and transverse directions within the truss girder are non-uniform because of the air flow inside the truss girder. For example, the air temperature close to the upper deck is higher than that close to the bottom deck during the daytime; and the air temperature in the south may be higher than that in the north in the winter. Therefore, different surfaces, such as deck plates, corrugated sheets, and cross frames, should adopt different air temperatures for convection. However, few air temperature sensors at the same height are inside the truss girder.

In this study, the air flow inside the bridge truss girder is calculated using computational fluid dynamics method. A two-dimensional FE model of the cross-section and the air inside the truss girder is established in FLUENT [22], as shown in Fig. 10. The model consists of 14,092 nodes and 13,114 triangles or quadrilaterals elements, among which 10,206 are air elements and the other 2,908 are solid elements. The air is considered as incompressible ideal gas with a specific gas capacity of 1006.43 J/kg/°C and thermal conductivity of 0.0242 W/m/°C. Other material properties are the same as those in Table 1. The calculation process considers external radiation and convection, as well as internal thermal convection, radiation, and conduction. The interface between the air and truss girder is treated as a coupled boundary. Internal radiation is calculated using the discrete ordinates model. The temperatures measured by sensors T1, D2, and D3 on the external air are utilized as the temperature boundaries for the interfaces between the interior and exterior air. These interfaces correspond to

Fig. 10 Two-dimensional FE model of bridge cross-section and the internal air
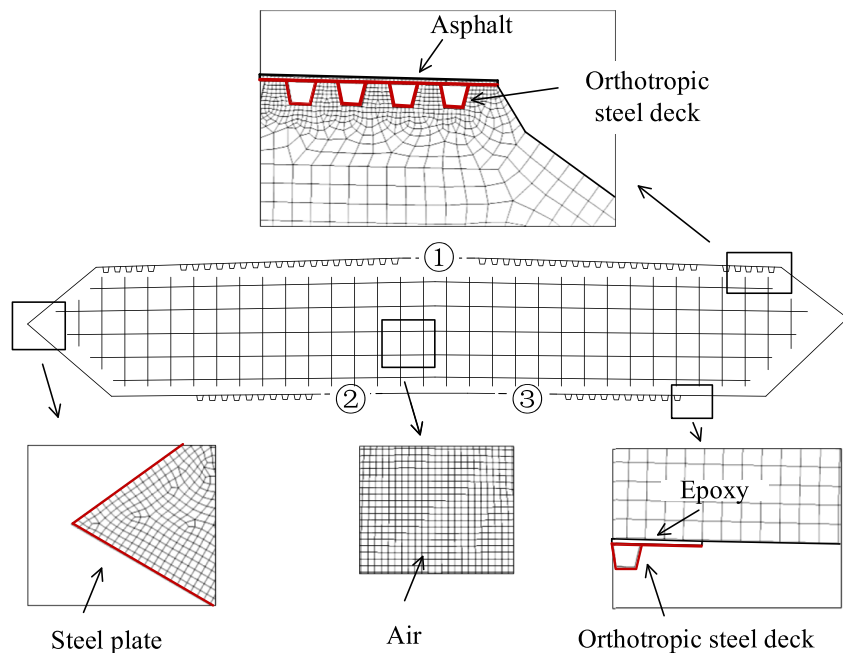
regions labeled as ①, ②, and ③ in Fig. 10. The air temperature inside the truss girder is calculated through a transient analysis in FLUENT.

Figure 11 shows the simulated distribution of the air temperature inside the girder at three representative instances on July 3, 2005. The air temperatures are relatively uniform across most of the interior space, with large temperature gradients adjacent to the interior girder surfaces. The air temperatures adjacent to the interior surfaces are higher than other locations. The maximum air temperature difference between the top and the bottom is 11.25 ℃, occurring at 17:00. Figure 12 presents the calculated air temperature at sensor D1 and compares it with the measurement. The air temperature rose from 07:00 to 16:00 and then decreased after 16:00. The calculated temperature at D1 shows a good agreement with the measurement. The root mean square error (RMSE) is 0.74 ℃ only. These results indicate the necessity and effectiveness of using the two-dimensional FE model to calculate the interior air temperature of the deck.
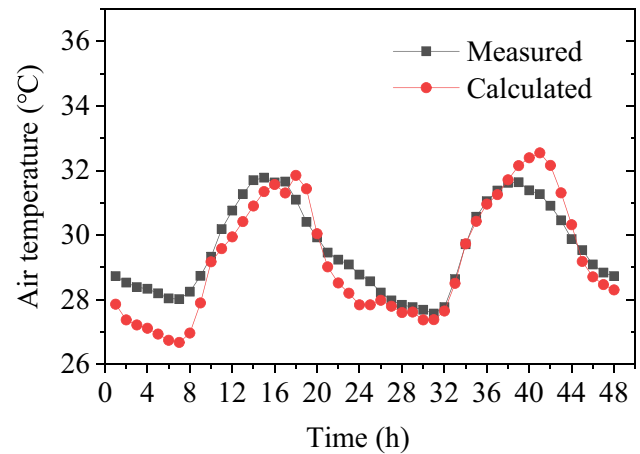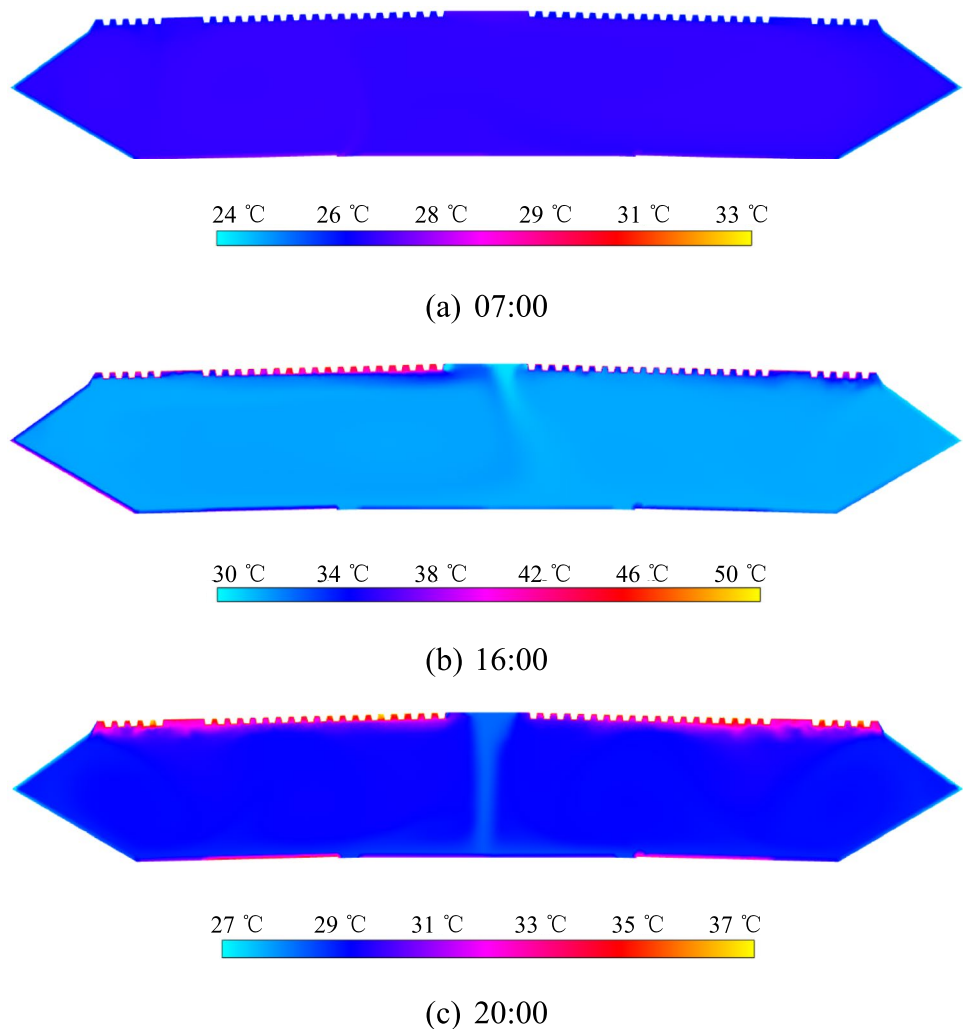

Fig. 12 Calculated and measured air temperatures at sensor D1

Fig. 11 Air temperature distribution at three representative instances on July 3, 2005. (**a**) 07:00. (**b**) 16:00. (**c**) 20:00


(a) 07:00

(b) 16:00

(c) 20:00

3.5 Thermal boundary conditions

On the exterior surfaces, the solar radiation, long-wave radiation, and heat convection are considered. Solar radiation is loaded onto the exterior surfaces of the bridge in the form of equivalent heat generation rate. The external air temperature for heat convection is given in Fig. 6, with the convection coefficients calculated from Eq. (4). The long-wave radiation on the exterior surface is calculated with Eq. (15).

On the interior surfaces, the long-wave radiation and heat convection are considered. The long-wave radiation between the interior surfaces of the bridge is achieved using radiation matrix AUX12 and superelement MATRIX50 in ANSYS [40]. For heat convection, the previous calculated air temperatures in FLUENT are applied to the interior surfaces using Eq. (3).

Then both external and internal boundary conditions are applied to the FE model in ANSYS for the heat transfer analysis. The calculated temperature of the bridge is compared with the measurements.

(a) Top cross frame (detail A)

(b) Bottom cross frame (detail B)
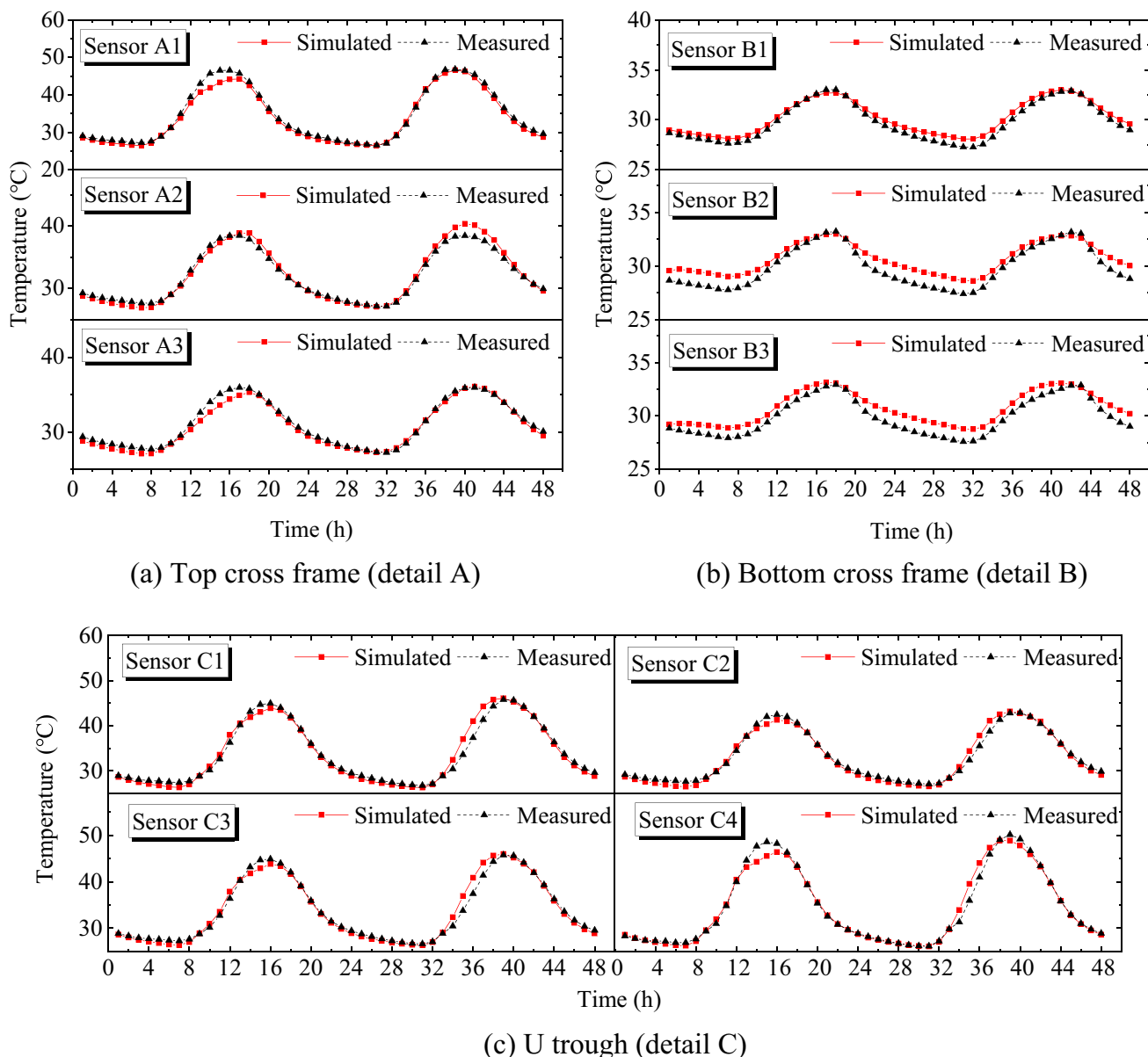
(c) U trough (detail C)

Fig. 13 Simulated and measured temperatures of the bridge girder. (**a**) Top cross frame (detail A). (**b**) Bottom cross frame (detail B). (**c**) U trough (detail C)

3.6 Temperature results

The calculated and measured temperatures of the ten sensors in details A, B, and C in section O are compared in Fig. 13, showing excellent agreement. The RMSEs between the simulated and measured results of the three details are 0.80 °C, 0.79 °C, and 1.05 °C, respectively. The errors are acceptable in practice, indicating the proposed approach can accurately calculate the temperature distribution of the bridge. The discrepancies may be due to differences between the environmental parameters measured at weather stations and the actual values on the Tsing Ma Bridge. In addition, the thermal parameters used in the FE model (such as the specific heat capacity, thermal conductivity, heat convection coefficient, etc.) may differ from the actual values of the bridge, causing the discrepancy in the calculated temperature.

4 Comparisons with existing approaches

In this section, three existing approaches to the thermal boundary conditions are applied to the Tsing Ma Suspension Bridge for the heat transfer analysis. The simulated temperature of the top and bottom cross frames and the U trough is also compared with the field measurements.

4.1 Approach 1

This approach is based on the equivalent air temperature and overall heat convection coefficient, which is the most widely adopted method for calculating temperature distribution of bridges [8, 28, 35].

In Eq. (2), q is composed of long-wave radiation q_r, solar radiation q_s, and thermal convection q_c. Long-wave radiation q_r can be simplified as [8]

$$q_r = h_r(T_a - T_s), \tag{17}$$

where h_r is the heat convection coefficient with air represented by [3]

$$h_r = \varepsilon[4.8 + 0.075(T_a - 5)]. \tag{18}$$

The simplified calculation is effective when the temperature difference between T_a and T_s is much lower than the two absolute temperatures. Then the total heat flow is.

$$q = h_c(T_a - T_s) + h_r(T_a - T_s) + \alpha I_s = h_{eq}(T_{eq} - T_s), \tag{19}$$

where T_{eq} is the equivalent air temperature and h_{eq} is the equivalent overall heat convection coefficient. They can be calculated as

$$T_{eq} = T_a + \frac{\alpha I_s}{h_{eq}}, \tag{20}$$

$$h_{eq} = h_r + h_c. \tag{21}$$

In this approach, the internal and external thermal boundary conditions are applied in the form of heat convection. For section O of the present bridge, the measurement of sensor D1 is adopted as the internal air temperature, and the bridge external air temperature is shown in Fig. 6.

The temperature distribution of the bridge is similarly calculated and shown in Fig. 14. The simulation results fluctuate like the measured temperature. However, the measured temperature lagged from the simulated counterpart by 3 h at the top cross beam and U trough, and by 2 h at the bottom cross frame. The maximum simulated temperature is also smaller than the measured one, with the difference of about 4 °C, 3 °C, and 1 °C for the top cross frame, U trough, and bottom cross frame, respectively. The RMSEs of details A, B, and C are 2.44 °C, 1.38 °C, and 3.58 °C, respectively.

The calculated temperature has a significant difference from the measurement, which is mainly because the temperature measured by sensor D1 inside the truss girder is used as equivalent air temperature on all bridge interior surfaces. Simplifying the internal and external long-wave radiation into heat convection can also cause inaccuracies.

4.2 Approach 2

To consider the non-uniform air temperature inside the bridge girder, Shan et al. [23] constructed a five-segment coefficient function with Fig. 15 to approximate air temperatures adjacent to bridge interior surfaces, based on measurements of an interior air temperature sensor. The function is multiplied by the measurements of the interior sensor to obtain updated temperatures as the internal convection air temperature for the heat transfer analysis. The process is repeated until the difference between the simulated and measured structural temperatures is minimized, resulting in the final updated air temperature.

For the Tsing Ma Suspension Bridge, sensor D1 is the interior air temperature sensor, and air temperature T close to the internal surface is updated as follows:

$$T(t) = C(t) \times T_{D1}(t), \tag{22}$$
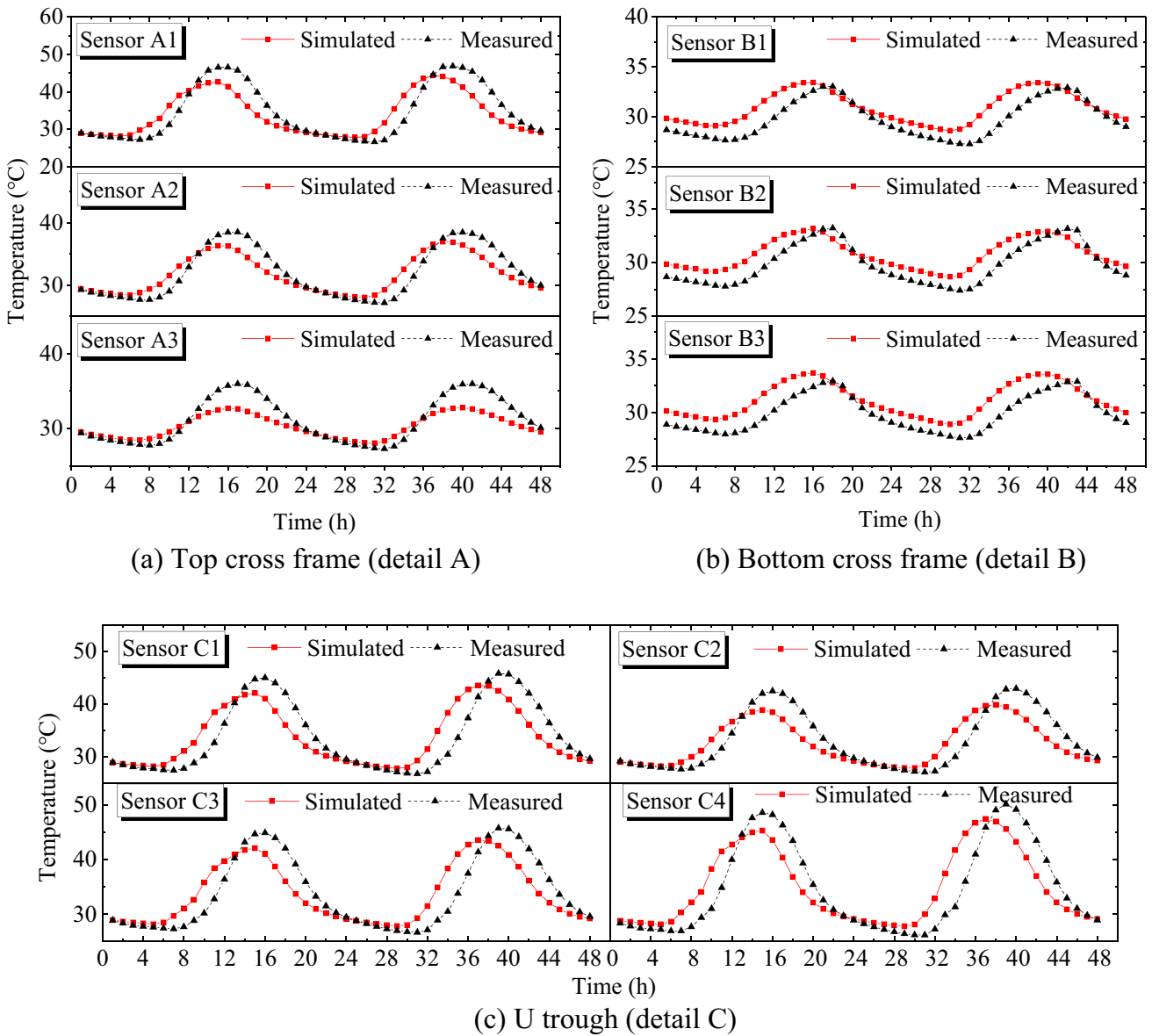
Fig. 14 Simulated and measured temperatures using Approach 1. (**a**) Top cross frame (detail A). (**b**) Bottom cross frame (detail B). (**c**) U trough (detail C)

where T_{D1} is the air temperature measurement of sensor D1 and $C(t)$ is the coefficient function defined into five segments as follows:

where [MnI, UpI, MxI, DwI] and [MnC, UpC, MxC, DwC] are the horizontal and vertical coordinates of the peak, valley, and two inflection points of curve $C(t)$, respectively.

$$C(t) = \begin{cases} (DwC - MnC) \times \sin\left[\frac{t+24-DwI+2\times(24-DwI+MnI)}{2\times(24-DwI+MnI)} \times \pi\right] + DwC & 0 \le t \le MnI \\ (UpC - MnC) \times \sin\left[\frac{t-UpI}{2\times(UpI-MnI)} \times \pi\right] + UpC & MnI < t \le UpI \\ (MxC - UpC) \times \sin\left[\frac{t-UpI}{2\times(MxI-UpI)} \times \pi\right] + UpC & UpI < t \le MxI \\ (MxC - DwC) \times \sin\left[\frac{t-MxI+(DwI-MxI)}{2\times(DwI-MxI)} \times \pi\right] + DwC & MxI < t \le DwI \\ (DwC - MnC) \times \sin\left[\frac{t-DwI+2\times(24-DwI+MnI)}{2\times(24-DwI+MnI)} \times \pi\right] + DwC & DwI \le t \le 24 \end{cases}, \tag{23}$$
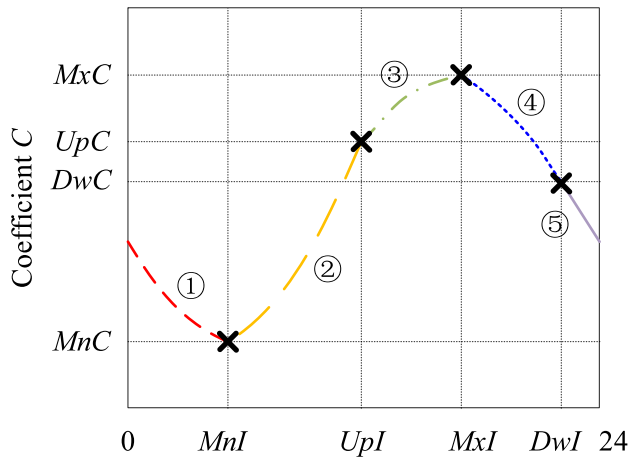
Fig. 15 Coefficient curve for updating bridge internal air temperatures in 1 day [23]

With the updated air temperature, the bridge's internal and external thermal boundary conditions can be calculated from Eqs. (20) and (21). The internal and external long-wave radiation are still simplified to heat convection. The simulated temperatures of the U trough and cross frames are compared with the measured ones in Fig. 16. The simulated results have no obvious phase difference. The RMSEs of details A, B, and C are 1.95 °C, 1.39 °C, and 2.83 °C, respectively.

In addition to the simplified long-wave radiation, another reason for the simulated discrepancies is that the ratio of air temperature near the interior surface of the bridge to the measurement of sensor D1 may not follow the sine function exactly. Moreover, the inflection points and peaks may also not correspond to the same time instants on different days.

4.3 Approach 3

This approach considers long-wave radiation between interior surfaces with Eq. (16), which was achieved using radiation matrix in ANSYS [40]. The heat convection between the air inside the bridge and the interior surfaces is not considered. Meanwhile, heat convection is still applied to the exterior surfaces.

By adopting this approach, the calculated and measured temperatures are shown in Fig. 17. The simulated results of the three details show the same fluctuation trends with the measured temperature, and no obvious phase differences are observed. However, the simulated temperatures are all greater than the measured ones. The RMSEs of details A, B, and C are 2.42 °C, 1.32 °C, and 3.28 °C, respectively. The simulation errors are mainly from neglecting thermal convection inside the bridge. The air flow inside the girder cannot be neglected because the Tsing Ma Suspension Bridge is a steel truss bridge with openings.

### 4.4 Result comparisons and discussions

The average RMSEs of the results of the proposed and the three existing approaches are 0.88 °C, 2.47 °C, 2.06 °C, and 2.34 °C, respectively. Among all approaches, the proposed one is the most accurate with the lowest RMSEs in the heat transfer analysis of the bridge.

The characteristics of the four approaches are summarized and compared in Table 2. Approach 1 considers the long-wave radiation as equivalent to heat convection and uses equivalent air temperature. It neglects the non-uniform temperature distribution inside the girder. This straightforward approach leads to significant phase differences between the simulated and measured temperatures. Approach 2 considers the non-uniform temperature distribution inside the bridge by constructing a sine function. However, it requires some measured structural temperatures to update the sine function. The approach also simplifies the internal and external long-wave radiation, causing inaccuracies. The accuracy of this approach relies on the selection of the four characteristic points of the sine function. Approach 3 accurately calculates the long-wave radiation between interior surfaces of the bridge while neglecting the interior heat convection. This neglect is appropriate for bridges without openings, such as box girder bridges, in which internal heat radiation dominates the heat transfer mechanism and heat convection is insignificant. The proposed approach considers the most accurate heat flow on the bridge interior and exterior surfaces and calculates the heat convection and heat radiation separately. It achieves the most accurate results.

5 Conclusion

Obtaining an accurate temperature distribution of a long-span bridge is necessary in investigating the temperature behavior of the bridge. This study proposes an accurate approach to simulate thermal boundary conditions used in the heat transfer analysis and compares the effectiveness with other three approaches. The calculated time-dependent temperatures of the bridge at different locations are compared with measured data from the Tsing Ma Suspension Bridge. The following conclusions can be drawn:

1. The study pioneers a new approach to calculate non-uniform air temperatures inside the bridge deck using computational fluid dynamics. It utilizes air elements to consider air flow inside the bridge girder and enables the calculation of air temperature adjacent to bridge interior surfaces. Long-wave radiation on the interior and exterior surfaces are calculated directly according to the Stefan–Boltzmann law. This approach provides
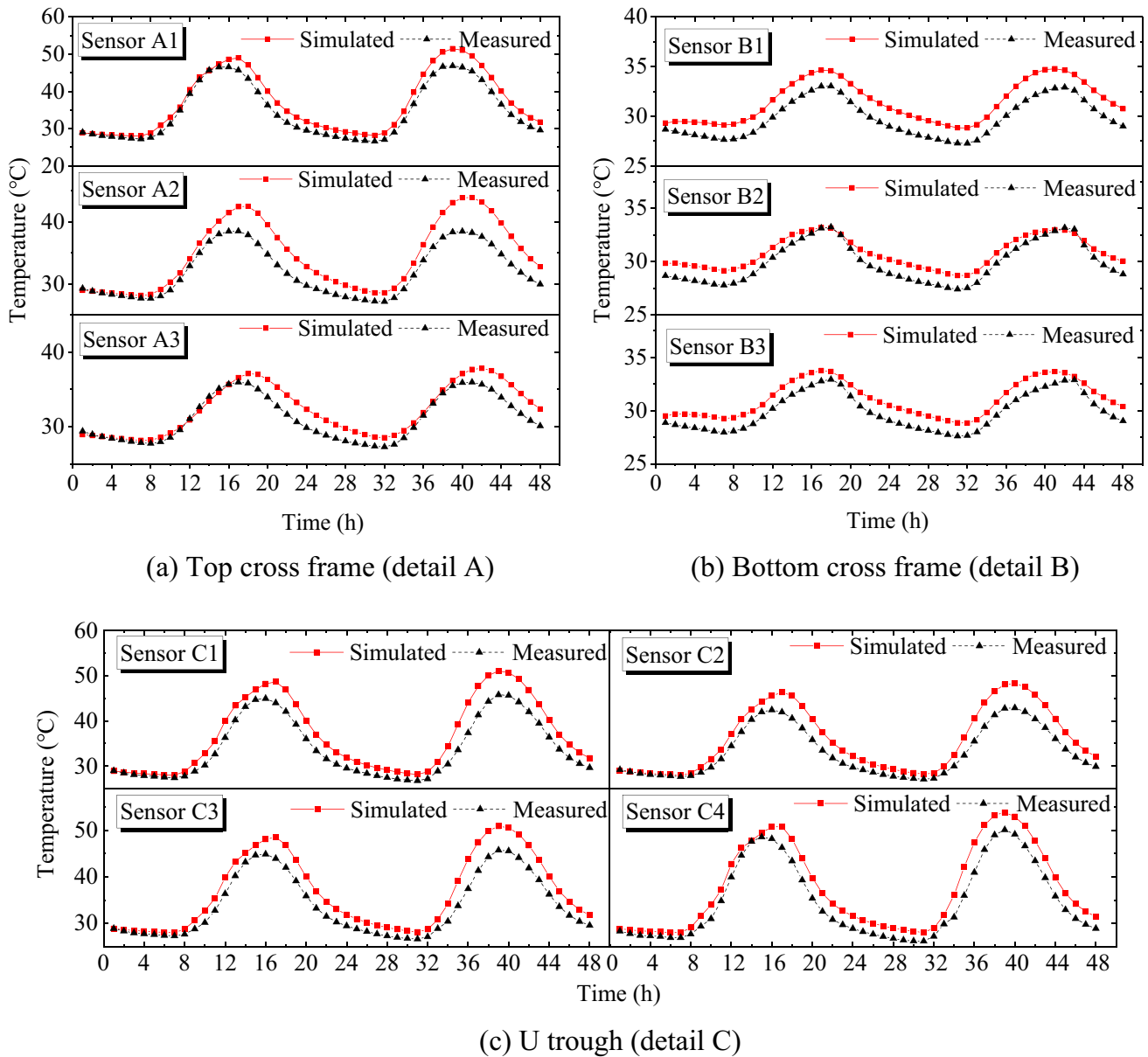
(a) Top cross frame (detail A)

(b) Bottom cross frame (detail B)
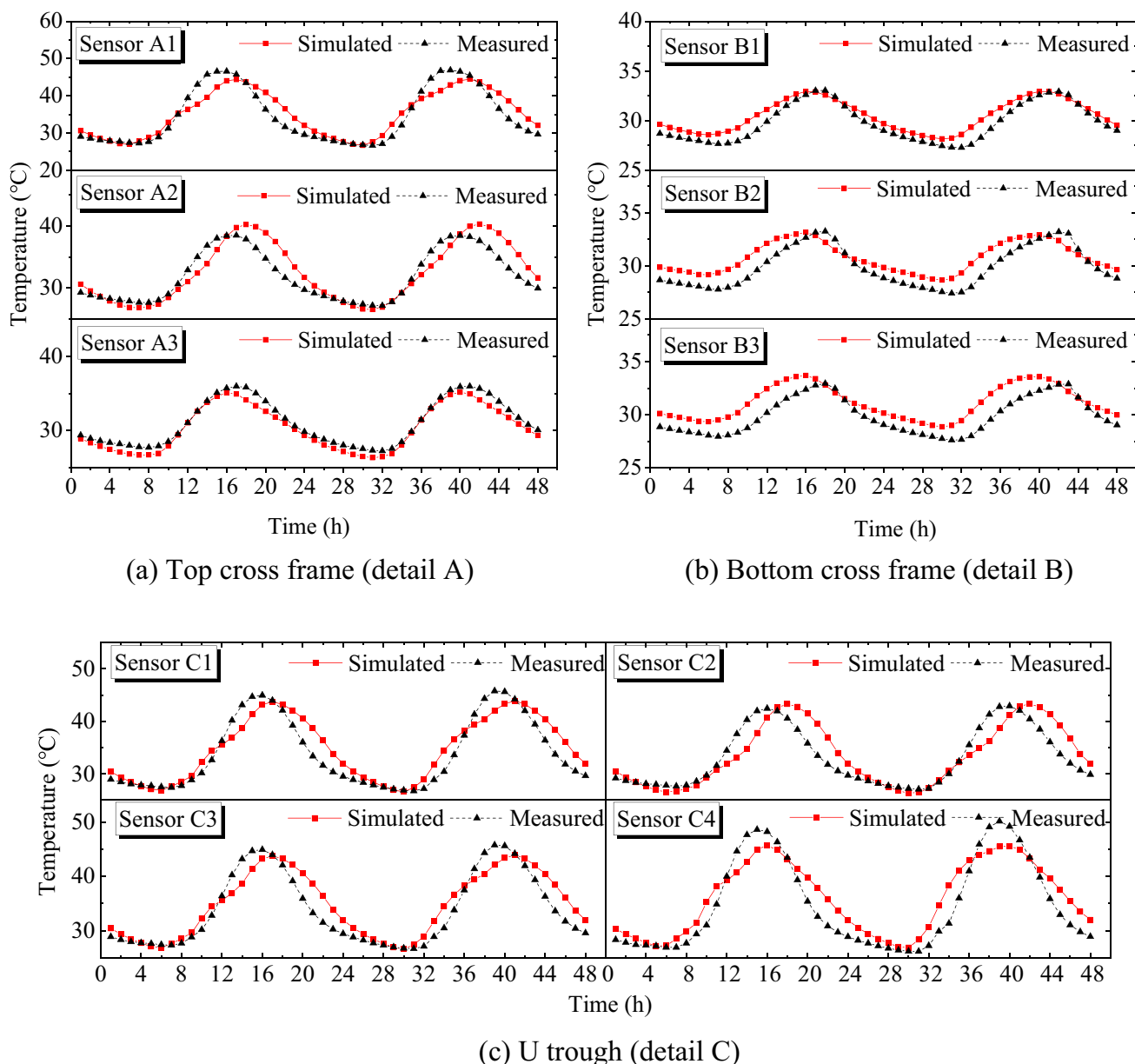
(c) U trough (detail C)

Fig. 16 Simulated and measured temperatures using Approach 2. (**a**) Top cross frame (detail A). (**b**) Bottom cross frame (detail B). (**c**) U trough (detail C)

a more reasonable means of ensuring accurate bridge temperature distribution.

2. Simplifying long-wave radiation to heat convection may introduce discrepancies. Approach 1, which simplifies the bridge's internal and external long-wave radiation, had the lowest accuracy with an average RMSE of 2.47 °C. The proposed approach accurately calculated the long-wave radiation from the ground, the atmosphere, and interior surfaces, and had the highest accuracy, with an average RMSE of 0.88 ℃.

3. Approaches considering non-uniform air temperature within the bridge's truss girder achieve better simula-

tion results. Approach 2 and the proposed approach show higher accuracy compared with approaches 1 and 3. The proposed approach calculates the detailed time-dependent air temperature distribution inside the truss girder in FLUENT and is the most effective one.

4. The study provides references for the temperature calculation of similar truss girder bridges. For box girder bridges, neglecting heat convection inside the box may cause insignificant errors.

(a) Top cross frame (detail A)

(b) Bottom cross frame (detail B)

(c) U trough (detail C)

Fig. 17 Simulated and measured temperatures using Approach 3. (**a**) Top cross frame (detail A). (**b**) Bottom cross frame (detail B). (**c**) U trough (detail C)

Table 2 Comparison of the four approaches to the thermal boundary condition

Approach	Interior		Exterior		
	Heat convection, q_c	Long-wave radiation, q_{tr}	Heat convection, q_c	Long-wave radiation, q_i	Solar radiation, q_i
1	$h_c\,(T_a - T_s)$	Simplified $h_r\,(T_a - T_s)$	$h_c\,(T_a - T_s)$	Simplified $h_r\,(T_a - T_s)$	αI_s
2	$h_c\,(T_a^* - T_s)$	Simplified $h_r\,(T_a^* - T_s)$			
3	/	$\tilde{q}_r^{12}$(Eq. (16))			
Proposed Approach	$h_c\,(T_a^a - T_s)$			q_r (Eq. (15))	

[*]Non-uniform air temperature inside the truss girder is considered by an iterative approach

[a]Non-uniform air temperature inside the truss girder is simulated in FLUENT

Declarations

Conflict of interest The authors have no relevant financial or non-financial interests to disclose.

References

1. Au FTK, Tong M, Tham LG (2001) Design thermal loading for steel bridges in Hong Kong. Transactions 8(2):1–9
2. Bergman TL, Bergman TL, Incropera FP, DeWitt DP, Lavine AS (2006) Fundamentals of heat and mass transfer, 6th edn. John Wiley & Sons, Hoboken, NJ
3. Branco FA (1986) Thermal effects on composite box girder bridges during construction. In: Proceedings of 2nd International Conference on Short and Medium Span Bridges, Canadian Society for Civil Engineering, Montreal, pp 215–226
4. Cao Y, Yim J, Zhao Y, Wang ML (2010) Temperature effects on cable stayed bridge using health monitoring system: a case study. Struct Health Monit 10(5):523–537
5. Cornwell P, Farrar CR, Doebling SW, Sohn H (1999) Structural testing series: Part 4. Exp Tech 23(6):45–48
6. De Battista N, Brownjohn JMW, Tan HP, Koo K (2015) Measuring and modelling the thermal performance of the Tamar Suspension Bridge using a wireless sensor network. Struct Infrastruct Eng 11(2):176–193
7. Deng Y, Ding Y, Li A (2010) Structural condition assessment of long-span suspension bridges using long-term monitoring data. Earthq Eng Eng Vib 9(1):123–131
8. Elbadry MM, Ghali A (1983) Temperature variations in concrete bridges. J Bridge Eng 109:2355–2374
9. Emerson M (1973) The calculation of the distribution of temperature in bridges. In: TRRL Report LR 561. Transport and Road Research Laboratory, Crowthorne
10. Froli M, Hariga N (1993) La risposta termica per effetti ambientali dei ponti a travata in ca cap. Atti delle' Associazione Italiana Cemento Armato e Precompresso Associazione Italiana Cemento Armato e Precompresso 93:161–170
11. Gu B, Zhou FY, Gao W, Xie FZ, Lei LH (2020) Temperature gradient and its effect on long-span prestressed concrete box Girder Bridge. Adv Civ Eng 2020:1–18
12. Hu J, Wang L, Song X, Sun Z, Cui J, Huang G (2020) Field monitoring and response characteristics of longitudinal movements of expansion joints in long-span suspension bridges. Measurement 162:107933
13. Huang S, Cai C, Zou Y, He X, Zhou T, Zhu X (2022) Experimental and numerical investigation on the temperature distribution of composite box girders with corrugated steel webs. Struct Control Health Monit 29(12):e3123
14. Iqbal M (2012) An introduction to solar radiation. Elsevier, Amsterdam
15. Kromanis R, Kripakaran P, Harvey B (2016) Long-term structural health monitoring of the Cleddau bridge: evaluation of quasi-static temperature effects on bearing movements. Struct Infrastruct Eng 12(10):1342–1355
16. Li H, Li S, Ou J, Li H (2009) Modal identification of bridges under varying environmental conditions: temperature and wind effects. Struct Control Health Monit 17:495–512
17. Li L, Chen B, Zhou L, Xia Q, Zhou Y, Zhou X, Xia Y (2023) Thermal behaviors of bridges—a literature review. Adv Struct Eng 26(6):985–1010
18. Lienhard JH (2003) A heat transfer textbook, 3rd edn. Phlogiston Press, Cambridge
19. Liu C, DeWolf JT (2007) Effect of temperature on modal variability of a curved concrete bridge under ambient loads. J Struct Eng 133(12):1742–1751
20. Mao J, Wang H, Feng D, Tao T, Zheng W (2018) Investigation of dynamic properties of long-span cable-stayed bridges based on one-year monitoring data under normal operating condition. Struct Control Health Monit 25(5):e2146
21. Martin M, Berdahl P (1984) Characteristics of infrared sky radiation in the United States. Sol Energy 33(3):321–336
22. Matsson JE (2023) An introduction to Ansys Fluent 2023. Sdc Publications, Mission, KS
23. Shan Y, Li L, Xia Q, Gao W, Jing Q, Xia Y (2023) Temperature behavior of cable-stayed bridges. Part I—global 3D temperature distribution by integrating heat-transfer analysis and field monitoring data. Adv Struct Eng 26(9):1579–1599
24. Sohn H, Dzwonczyk M, Straser EG, Kiremidjian AS, Law KH, Meng T (1999) An experimental study of temperature effect on modal parameters of the Alamosa Canyon Bridge. Earthq Eng Struct D 28(8):879–897
25. Sousa Tomé E, Pimentel M, Figueiras J (2018) Structural response of a concrete cable-stayed bridge under thermal loads. Eng Struct 176:652–672
26. Tong M, Tham LG, Au FTK (2002) Extreme thermal loading on steel bridges in tropical region. J Bridge Eng 7(6):357–366
27. Wang C, Ansari F, Wu B, Li S, Morgese M, Zhou J (2022) LSTM approach for condition assessment of suspension bridges based on time-series deflection and temperature data. Adv Struct Eng 25(16):3450–3463
28. Wang D, Liu Y, Liu Y (2018) 3D temperature gradient effect on a steel-concrete composite deck in a suspension bridge with field monitoring data. Struct Control Health Monit 25(7):e2179
29. Wang G, Ding Y, Liu X (2019) The monitoring of temperature differences between steel truss members in long-span truss bridges compared with bridge design codes. Adv Struct Eng 22(6):1453–1466
30. Wang Y, Zhan Y, Zhao R (2016) Analysis of thermal behavior on concrete box-girder arch bridges under convection and solar radiation. Adv Struct Eng 19(7):1043–1059
31. Westgate R, Koo K, Brownjohn J (2015) Effect of solar radiation on suspension bridge performance. J Bridge Eng 20(5):04014077
32. Whitaker S (1977) Fundamental principles of heat transfer. Pergamon Press, New York
33. Xia Q, Wu W, Li F, Zhou X, Xu Y, Xia Y (2022) Temperature behaviors of an arch bridge through integration of field

monitoring and unified numerical simulation. Adv Struct Eng 25(16):3492–3509

34. Xia Q, Zhang J, Tian Y, Zhang Y (2017) Experimental study of thermal effects on a long-span suspension bridge. J Bridge Eng 22(7):04017034

35. Xia Y, Chen B, Zhou X, Xu Y (2013) Field monitoring and numerical analysis of Tsing Ma Suspension Bridge temperature behavior. Struct Control Health Monit 20(4):560–575

36. Xu YL, Chen B, Ng CL, Wong KY, Chan WY (2009) Monitoring temperature effect on a long suspension bridge. Struct Control Health Monit 17(6):632–653

37. Xu YL, Xia Y (2012) Structural health monitoring of long-span suspension bridges. CRC Press, London

38. Yang D, Yi T, Li H, Zhang Y (2018) Monitoring and analysis of thermal effect on tower displacement in cable-stayed bridge. Measurement 115:249–257

39. Yang X, Zhang J, Ren W (2017) Temperature effect analysis of a long-span cable-stayed bridge based on extreme strain estimation. Smart Struct Syst 20(1):11–22

40. Zhou L, Xia Y, Brownjohn JMW, Koo KY (2016) Temperature analysis of a long-span suspension bridge based on field monitoring and numerical simulation. J Bridge Eng 21(1):04015027

41. Zhou Y, Xia Y, Sun Z, Fujino Y (2022) Analytical formulation of the temperature-induced deformation of multispan suspension bridges. Struct Control Health Monit 29(6):e2937

42. Zhu J, Meng Q (2017) Effective and fine analysis for temperature effect of bridges in natural environments. J Bridge Eng 22(6):04017017

43. Zhu Q, Wang H, Mao J, Wan H, Zheng W, Zhang Y (2020) Investigation of temperature effects on steel-truss bridge based on long-term monitoring data: case study. J Bridge Eng 25(9):05020007

44. Zuk W (1965) (1965) Thermal behavior of composite bridges—insulated and uninsulated. Highway Res Rec 76:231–253

Publisher's Note Springer Nature remains neutral with regard to jurisdictional claims in published maps and institutional affiliations.